

The eclipsing novalike cataclysmic variable CRTS SSS100505 J093417-174421

RAYMUNDO BAPTISTA,¹ ALBERT BRUCH,² RAIMUNDO LOPES DE OLIVEIRA,^{3,4,5} CLÁUDIA V. RODRIGUES,⁶
ALEXANDRE S. OLIVEIRA,⁷ AND ISABEL J. LIMA⁸

¹*Departamento de Física, Universidade Federal de Santa Catarina, Campus Trindade, 82912-600 Florianópolis - SC, Brazil*

²*Laboratório Nacional de Astrofísica, Rua Estados Unidos, 154, 37504-364 Itajubá - MG, Brazil*

³*Departamento de Física, Universidade Federal de Sergipe, Av. Marechal Rondon S/N, 49100-000 São Cristóvão - SE, Brazil*

⁴*Observatório Nacional, Rua Gal. José Cristino, 77, 20921-400 Rio de Janeiro - RJ, Brazil*

⁵*Departamento de Astronomia, Instituto de Astronomia, Geofísica e Ciências Atmosféricas da USP, Cidade Universitária, 05508-900 São Paulo, SP, Brazil*

⁶*Divisão de Astrofísica, Instituto Nacional de Pesquisas Espaciais, 12227-010 São José dos Campos - SP, Brazil*

⁷*IP&D, Universidade do Vale do Paraíba, 12244-000 São José dos Campos - SP, Brazil*

⁸*Universidade Estadual Paulista, Campus de Guaratinguetá, Av. Dr. Ariberto Pereira da Cunha, 333 12516-410 Guaratinguetá - SP, Brazil*

ABSTRACT

Time-resolved optical photometry, complemented by TESS data and long-term survey light curves, reveals that the transient object CRTS SSS100505 J093417-174421 is an eclipsing novalike cataclysmic variable of the VY Scl subtype, with an orbital period of 0.16329188(8) d. An analysis of the light curves with eclipse mapping techniques and an entropy landscape procedure indicates an orbital inclination of 81.5° and a mass ratio of 0.45. Eclipse maps reveal two diametrically opposed asymmetric arcs of enhanced emission in the intermediate and outer regions of an accretion disk elongated in the direction perpendicular to the line joining both stars, interpreted as tidally-induced spiral shock arms. The accretion disk is 50 per cent larger in the longer wavelength TESS data than in the optical range, in line with the expected radial temperature gradient of an opaque steady-state disk. The combination of a small optical disk radius (of 21 per cent of the orbital separation) and high orbital inclination explains the relatively faint absolute magnitude of $M_g = 7.44$ for a novalike variable.

Keywords: (stars:) binaries: close – (stars:) binaries: eclipsing – (stars:) novae, cataclysmic variables

1. INTRODUCTION

The foundational model of cataclysmic variables (CVs), developed during the 1960s and 1970s and summarized in the excellent early reviews by Warner (1976) and Robinson (1976), has been robustly validated and continually refined over the following decades. The accumulated knowledge about CVs ~20 years later is assessed in Warner's (1995) comprehensive monograph. But then the field has grown so vast that subsequent reviews are all limited to specific topics. CVs are interacting binary systems, where a late-type star (the secondary) fills its Roche lobe and transfers mass to a more massive and evolved companion, a white dwarf (WD). The dynamics of the mass transfer are primarily deter-

raybap@gmail.com

albert@lna.br

raimundo.lopes@academico.ufs.br

claudia.rodrigues@inpe.br

alexandre@univap.br

isabellima01@gmail.com

mined by the mass transfer rate and the magnetic field strength of the WD. The interaction between the infalling material and the magnetic field of the WD is the main mechanism that determines whether an accretion disk – either fully developed or disrupted in its central regions – can form or not.

Over the last half century, the number of known or suspected CVs has increased dramatically, from a few dozen to several thousand. This growth has been driven by large-scale survey projects such as the Sloan Digital Sky Survey (SDSS; York et al. 2000), Catalina Real-Time Transient Survey (CRTS; Drake et al. 2009), All-Sky Automated Survey for Supernovae (ASAS-SN; Kochanek et al. 2017), and Zwicky Transient Facility (ZTF; Bellm et al. 2019; Masci et al. 2019). Many of those objects have never been studied in greater detail, such that often not more than a fragmentary light curve or a single spectrum are available. A deeper study of a larger number of objects is crucial for addressing the many open questions in the field. For example, the evolutionary pathways and the connection between physical properties (e.g., Zorotovic & Schreiber 2020; Schaefer 2024), or the origin and evolution of magnetic fields in WDs (e.g., Briggs et al. 2018; Schreiber et al. 2021), remain major unresolved issues.

Another important question concerns the detailed accretion flow and the structure of the accretion disk in CVs. Here, indirect imaging techniques provide valuable information. Based on the time dependent structure and radial velocity variations of spectral lines, Doppler tomography (Marsh 2001) permits the reconstruction of the distribution of line emission in a CV. In eclipsing systems, a detailed analysis of the eclipse profile allows an even more detailed view. The Eclipse Mapping Method, first introduced by Horne (1985), transforms the shape of the eclipse light curve into a map of the surface brightness distribution of the occulted regions. Past applications of this technique to the investigation of the structure, the spectrum, and the time evolution of accretion disks in CVs have enriched our understanding of these structures with a wealth of details. These include moving heating/cooling waves during outbursts in dwarf novae, tidally-induced spiral shocks of emitting gas with sub-Keplerian velocities, elliptical precessing disks associated with superhumps, and measurements of the radial run of the disk viscosity through the mapping of the disk flickering sources. For reviews about this technique and its previous applications and results, see Baptista (2001, 2016).

One of the systems that has so far remained largely unstudied is CRTS SSS100505 J093417-174421 (hereafter CRTS J0934), identified as a transient by the CRTS.

Based on its long-term CRTS light curve, Oliveira et al. (2020) included the object in their spectroscopic search for magnetic CVs. Its spectrum exhibits the typical features of a CV, namely strong hydrogen Balmer emission lines along with weaker helium emission lines. If the broad (FWHM = 2300 km/s) feature around 4960 Å in their spectrum does indeed include a significant contribution from He II 4686 Å, its equivalent ratio to H β is nevertheless too low to satisfy the empirical criteria (Silber 1992) for a classification as a magnetic CV. The initial assumption is that CRTS J0934 is similar to many other non-magnetic CVs, probably of the novalike subtype, since the long-term light curve does not reveal dwarf-nova outbursts (see Sect. 3).

Here, we present a photometric follow-up of CRTS J0934 that reveals the system to be eclipsing. We also carry out a detailed analysis of its accretion disk using maximum-entropy eclipse mapping techniques.

2. OBSERVATIONS

We observed CRTS J0934 during 16 nights between 2021, April 9 and June 18 at the 1.6 m Perkin Elmer (PE) and the 0.6 m Boller & Chivens (BC) telescopes of the *Observatório do Pico dos Dias* (OPD), Brazil. A summary is given in Table 1. To characterize light variations on time scales between hours and seconds, we aimed to maximize the total duration of the light curves and the time resolution while maintaining a signal-to-noise ratio sufficient to preserve details of variations. Therefore, most observations were taken in white light, which leads to an effective wavelength roughly similar to the Johnson V-band (Bruch 2018). Integration times between 5 and 10 s at the larger telescope and of 60 s at the smaller one were chosen. Together with a read-out time of 2 s this resulted in the time resolution cited in the table.

Data reduction followed the usual standard procedures. Simple aperture photometry was performed relative to the primary comparison star UCAC4 362-054814 (Zacharias et al. 2013), the constancy of which was verified using 4 other comparison stars in the field. The average magnitudes quoted in Table 1 are rough estimates, calculated by adding the V magnitude of the comparison star as quoted in the UCAC4 catalogue to the mean of the nightly differential white light magnitude between the target and the comparison star (excluding eclipses). Magnitudes were thus not reduced to a standard photometric system, and their absolute values are not of high precision. However, magnitude differences between different nights should be more reliable. All time stamps were transformed into Barycentric

Table 1. Journal of observations at OPD

Date	Start	ΔT^a	N^b	Δt^c	av.	Tel. ^d
2021	(UT)	(min)		(sec)	mag.	
Apr 09	00:34	138	673	12	17.97	PE
Apr 10	00:19	166	714	12	18.13	PE
Apr 11	00:03	159	1263	7	18.08	PE
Apr 11	23:59	174	1439	8	18.13	PE
Apr 19	22:52	203	189	62	18.02	BC
Apr 20	22:07	288	220	62	18.06	BC
Apr 21	21:35	318	306	62	18.19	BC
Apr 22	21:37	320	305	62	18.28	BC
Apr 28	21:38	308	300	62	18.33	BC
Apr 29	21:39	249	201	62	18.27	BC
Apr 30	21:25	256	206	62	18.44	BC
May 01	21:34	131	118	62	18.18	BC
May 02	21:33	277	270	62	18.25	BC
May 18	21:51	201	173	62	18.20	BC
Jun 17	21:27	102	100	62	18.24	BC
Jun 18	21:14	88	87	62	18.16	BC

^a: total time base;

^b: number of integrations;

^c: time resolution;

^d: PE = 1.6m Perkin Elmer; BC = 0.6m Boller & Chivens

Julian Date on the Barycentric Dynamical Time scale, using the on-line tool of [Eastman et al. \(2010\)](#).

CRTS J0934 was also observed by the Transiting Exoplanet Survey Satellite (TESS; [Ricker et al. 2014](#)) and data are available in the mission’s public archive. TESS observes sectors of the sky almost continuously during two spacecraft orbits, spanning about 27 days, only interrupted during short intervals for data download to Earth. The photometry is conducted in a broad pass-band, from 600 to 1000 nm, centered on the Cousins *I* band. The public TESS data of CRTS J0934 were downloaded from the Mikulski Archive for Space Telescopes (MAST) portal.¹ The system was observed in four sectors (see Table 2). Light curves from sectors 8 and 35 were extracted using the LIGHTKURVE² package. Those of sectors 62 and 89 are available at the MAST site as pre-reduced light curves. Simple aperture photometry (SAP) data were used. Details are listed in Table 2. CRTS J0934 does not have neighbors closer than $\approx 40''$. Therefore, even considering the large projected pixel size of TESS, contamination of the light curves is expected

¹ <https://mast.scsci.edu/portal/Mashup/Clients/Mast/Portal.html>

² <https://docs.lightkurve.org/index.html>

Table 2. Journal of TESS observations

TESS	Start	End	Number of	Δt
sector	(BJD)	(BJD)	exposures	(min)
08	2458517.37	2458541.99	894	30
35	2459255.00	2459279.98	2815	10
62	2459988.45	2460014.16	18047	2
89	2460718.14	2460746.85	19730	2

to remain small. In any case, its effect on the following analysis is negligible, as the TESS data were used to determine eclipse epochs, width, and shape, which are unaffected by additive contamination on timescales longer than the orbital period.

To investigate the long-term behavior of CRTS J0934 over approximately 15 years, we also retrieved its light curves from the CRTS and ZTF. They cover the period from 2005 to 2015 (CRTS), and from 2019 to 2024 (ZTF).

3. LIGHT CURVES AND ECLIPSE EPHEMERIS

The long-term light curve of CRTS J0934 is shown in Fig. 1a. The black and green dots are CRTS and ZTF *g*-band data, respectively. The red dots represent average nightly (out-of-eclipse) magnitudes of the OPD observations. The black arrows indicate mid-epochs of the TESS data. No attempt has been made to adjust the different photometric systems because this is not relevant to the purposes of this work. CRTS J0934 typically remained at a magnitude slightly fainter than 18 mag, occasionally brightening by about half a magnitude, but sometimes exhibiting low states as faint as nearly 21 mag (noting that only a few of the faint data points in the figure correspond to eclipse phases). No dwarf-nova outbursts were observed. Such behavior is consistent with novalike CVs of the VY Scl subtype (e.g., [Leach et al. 1999](#); [Duffy et al. 2024](#)).

On time scales of minutes (see Fig. 1b for an example), CRTS J0934 is characterized by strong flickering with an amplitude on the order of 0.3 mag, typical for VY Scl stars ([Bruch 2021](#)). On longer timescales, however, eclipses are the dominant feature, with 10 events recorded in the OPD light curves. Their average profile is shown in Fig. 3a as green dots with error bars. The eclipse epochs were determined by the minimum of a fit of a fifth-order polynomial to the profiles, allowing us to derive a preliminary orbital period. As an example of the photometric behavior of CRTS J0934 over several days, its sector 35 TESS light curve is displayed in Fig. 1c. Here, the red dots are average values in 1 d intervals after masking eclipses. Irregular variations on daily time scales occur, as is common in nova-

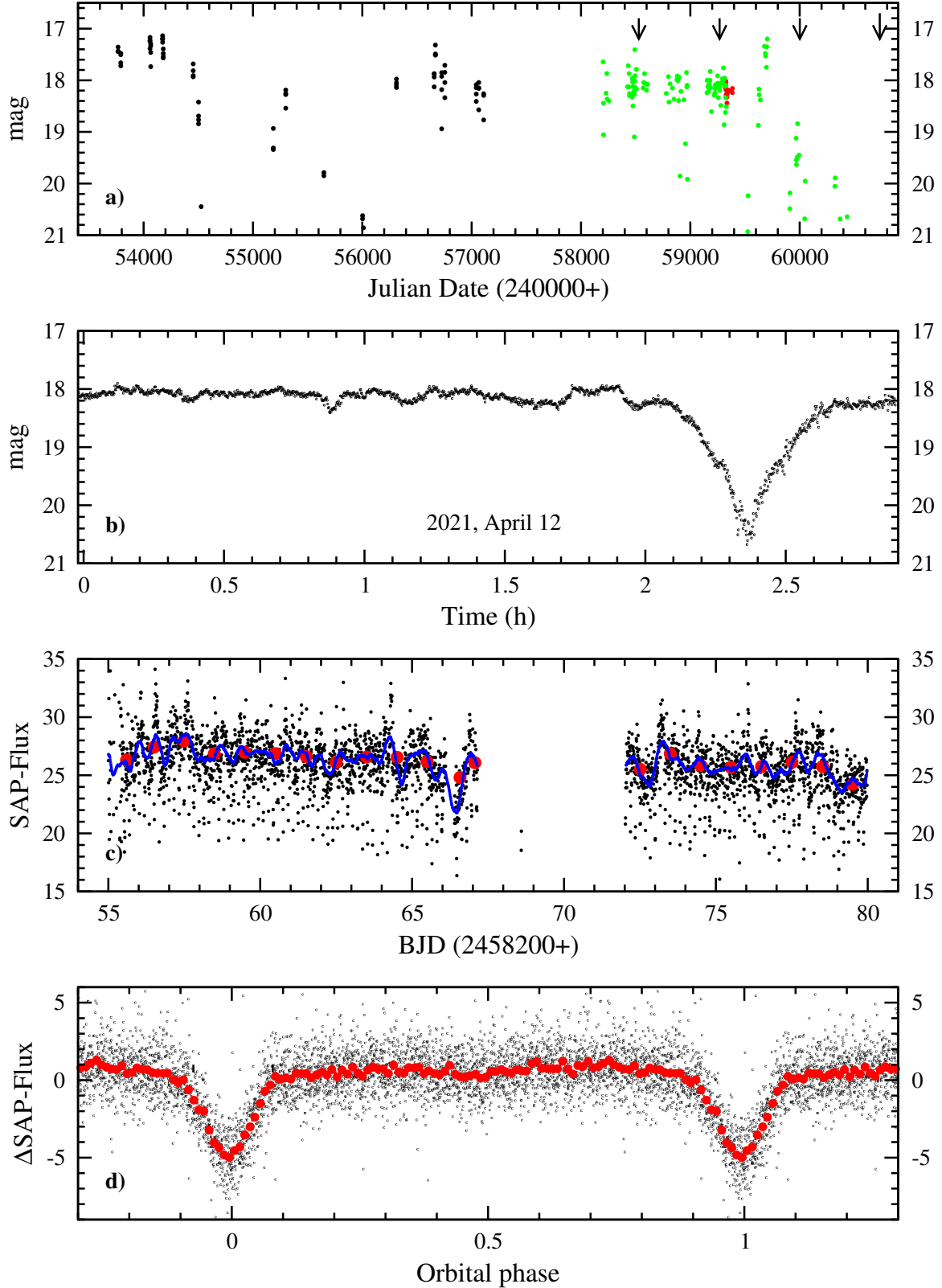


Figure 1. *a)* Long-term light curve of CRTS 0934. Black and green dots are CRTS and ZTF data, respectively. The red dots represent the nightly average out-of-eclipse magnitude of the OPD observations. The black arrows indicate mid-epochs of the TESS data. *b)* Time-resolved OPD light curve of 2021, April 12 (starting just before midnight of April 11). *c)* Sector 35 TESS light curve. The red dots are average flux values (after masking eclipses) within 1 d intervals. The light curves smoothed with a Savitzky-Golay filter (again, eclipses masked) are shown in blue. *d)* Combined TESS light curve of sectors 8 and 35, folded on the orbital period (small black dots). The red dots represent average values in phase bins of width 0.01.

Table 3. Eclipse epochs

Ecl. number	Ecl. epoch BJD (2400000+)	Telescope
-5000	58500.1449	TESS
-714	59200.0131	TESS
0	59316.6028	PE
55	59325.5849	BC
61	50326.5646	BC
67	59327.5429	BC
103	59333.4227	PE
104	59333.5867	BC
110	59334.5665	BC
116	59335.5462	BC
128	59337.5044	BC
226	59353.5065	BC
4112	59988.0582	TESS
8383	60718.1389	TESS

like CVs (see, e.g., Appendix A of Bruch 2024a). The TESS light curves are too noisy to measure individual eclipse epochs. Even more than in the earlier sectors, this is the case for sectors 62 and 89. CRTS J0934 was observed in a low state or in the transition into a low state (Fig. 1a) in Sector 62. The high noise level in sector 89 suggests that the system did not yet recover from the low state after the last ZTF data point. Although individual eclipse epochs cannot be measured in the TESS light curves, folding the data on the preliminary period yields an average orbital light curve with clearly visible eclipses, as is shown in Fig. 1d for the combined sectors 8 and 35 data. Before phase-folding, a smoothed version of the light curves (shown in blue for the sector 35 light curve in Fig. 1c) was subtracted from the original data to remove variations on supraorbital time scales. This version was obtained using a Savitzky-Golay (Savitzky & Golay 1964) filter with a cutoff time scale of 1 d and a 4th order smoothing polynomial. The folded light curves enable the determination of eclipse epochs for each sector with no cycle count ambiguities, extending the total time base greatly. They are listed in Table 3. All eclipse epochs together then yield the eclipse ephemeris

$$T_{\min} = BJD\ 2459316.6035(2) + 0.16329188(8) \times E, \quad (1)$$

where E is the cycle number.

4. ECLIPSE TOMOGRAPHY

We apply maximum-entropy eclipse mapping techniques to average OPD and TESS eclipse light curves of CRTS J0934. This analysis allows us to derive the surface brightness distribution of its accretion disk at two

different wavelengths and the uneclipsed component of the light curves (light from the secondary star and/or a vertically-extended disk wind), as well as to identify and investigate structures within the disk.

As a first step, we obtained average OPD and TESS light curves. The OPD data cover a relatively short time span in which CRT J9034 was in its typical brightness level and consistently showed the same eclipse shape. To improve the signal-to-noise and to minimize the influence of flickering for the subsequent analysis, the individual OPD light curves were phase-folded according to the ephemeris of Eq. (1) and combined in an average eclipse light curve with a resolution of 0.005 in phase. No data segment was removed and no filtering was applied to the OPD data before combining the light curves. A median flux was computed for each phase bin; the median of the absolute deviations with respect to the median was taken as the corresponding uncertainty at each bin. The resulting average light curve has signal-to-noise ratios ranging from $S/N \simeq 40$ (out-of-eclipse) to $\simeq 15$ (mid-eclipse). A similar procedure was applied to the combined TESS light curve of the sectors 8 and 35. In this case, we compensated for the subtraction of a smoothed version of the light curves before phase-folding (see Fig. 1c) by adding an arbitrary offset to the data in order to ensure positive fluxes across the eclipse.³ The data were further renormalized to a unity flux eclipse depth before computing the median flux at each phase bin. The resulting average TESS light curve has lower signal-to-noise, ranging from $S/N = 20$ (out-of-eclipse) to $\simeq 7$ (mid-eclipse). Because of the arbitrary offset added to the average TESS light curve, the uneclipsed component in this case is meaningless. Hereafter, we will refer to the average OPD and TESS light curves, respectively, as the V-band and I-band light curves to emphasize their different wavelengths.

Second, the eclipse geometry for the image reconstructions needs to be selected. The eclipse geometry is defined by a pair of values of the orbital inclination i and the mass ratio $q = M_2/M_1$ (where M_1 is the WD mass and M_2 is the secondary star mass) or, alternatively, the duration $\Delta\phi$ of the eclipse of the disk center. For a fixed $\Delta\phi$ value, there is a unique relation between i and q (Bailey 1979; Horne 1985). In low- \dot{M} systems, such as quiescent dwarf novae, $\Delta\phi$ can be directly measured from the light curve by the ingress/egress phases of the WD eclipse. However, in novalike systems such as CRTS J0934, the accretion disk is much brighter than

³ The logarithmic definition of entropy in the eclipse mapping method (Horne 1985) requires intensities in the eclipse map and fluxes in the light curves to always be positive numbers.

the WD and veils its contribution to the eclipse shape. In these cases, $\Delta\phi$ can be estimated from the eclipse full width-at-half depth (FWHD), or the full width-at-half maximum flux level (FWHM). This is based on the notion that the shadow of the secondary star covers about half of the entire disk when the disk center is just eclipsed or just reappeared from eclipse (FWHM) or, alternatively, that at these phases it covers about half of all the light that is hidden during eclipse minimum (FWHD). From the higher S/N, average V-band light curve of CRTS J0934, we estimate FWHD = 0.078 and FWHM = 0.087 (in units of the orbital period).

This estimate can be further improved with an “entropy landscape” procedure (e.g., Baptista et al. 2016). For a given $\Delta\phi$ value, the surface brightness distribution is skewed towards (away from) the L1 point if the inclination is underestimated (overestimated). Therefore, an incorrect inclination increases the amount of structure and the deviations from axi-symmetry of the eclipse map, which is flagged with a lower entropy value. Hence, the best choice for the eclipse geometry can be inferred by computing eclipse maps for a range of (i, q) values and finding the pair of values that yields the eclipse map of highest entropy. We again used the V-band light curve for this procedure. The results of the entropy landscape are shown in Fig. 2. The location of highest entropy is marked by a red cross. The maximum-entropy geometry parameters are $i = 81.5^\circ \pm 1.0^\circ$ and $q = 0.45 \pm 0.05$, corresponding to an eclipse width of $\Delta\phi = 0.085 \pm 0.003$ in phase, consistent with the range for these parameters inferred from the eclipse FWHD and FWHM estimates. This (i, q) pair of values will be adopted hereafter.

4.1. The CRTS J0934 eclipse maps

We use an eclipse map consisting of a flat Cartesian grid in the orbital plane centered on the position of the WD, with 51×51 pixels and side $2R_{L1}$ (where R_{L1} is the distance from the disk center to the inner Lagrangian point L1). Our eclipse mapping code implements a scheme of double default functions, D_+D_- , by simultaneously steering the solution towards the most nearly axi-symmetric map consistent with the data (D_+) and away from the crisscrossed arcs along the edges of the shadow of the occulting secondary star (D_-) (Spruit 1994; Baptista et al. 2005). It is optimized to recover asymmetric structures such as spirals arms (see, e.g., Harlaftis et al. 2004). The positive default function is a polar Gaussian with radial and azimuthal blur widths respectively of $\Delta r = 0.02 R_{L1}$ and $\Delta\theta = 20^\circ$ in order to minimize the azimuthal smearing effect and to improve

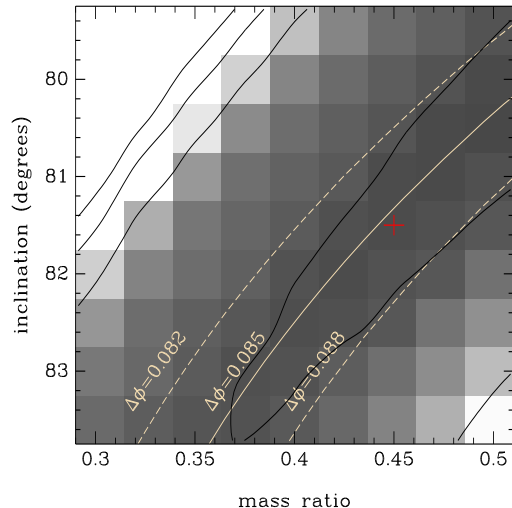


Figure 2. Entropy landscape in the (i, q) binary parameter plane. The entropy of the eclipse maps are shown as different shades of gray; darker regions have higher entropy. Contour lines indicate the shape of the entropy landscape and a red cross marks the location of highest entropy. White curves show lines of constant $\Delta\phi$ values.

the reconstruction of asymmetric sources.⁴ The negative default function is a Gaussian along the ingress/egress arcs of phase width $d\phi = 0.01$.

Because this version of the eclipse mapping method does not take into account for out-of-eclipse brightness changes, these were removed by dividing the average light curve by the best-fit spline function to the out-of-eclipse portion of the light curve, and scaling the result to the average out-of-eclipse flux level. With the assumption that the eclipse mapping model provides a complete description of the data, the error bars were further uniformly scaled to ensure a reduced $\chi^2 = 1$ for the reconstructions.⁵ The resulting light curves are shown in the left-hand panels of Fig. 3 as green dots. They show the characteristic double-stepped shape seen in the light curves of IP Peg in outburst, indicating the progressive occultation of two brightness sources, none of which coincide with disk center.

⁴ This choice for $\Delta\theta$ implies that any off-center point source is smeared in azimuth by $\simeq 60^\circ$.

⁵ This also ensures that the Monte Carlo procedure properly evaluates the uncertainties in the eclipse map.

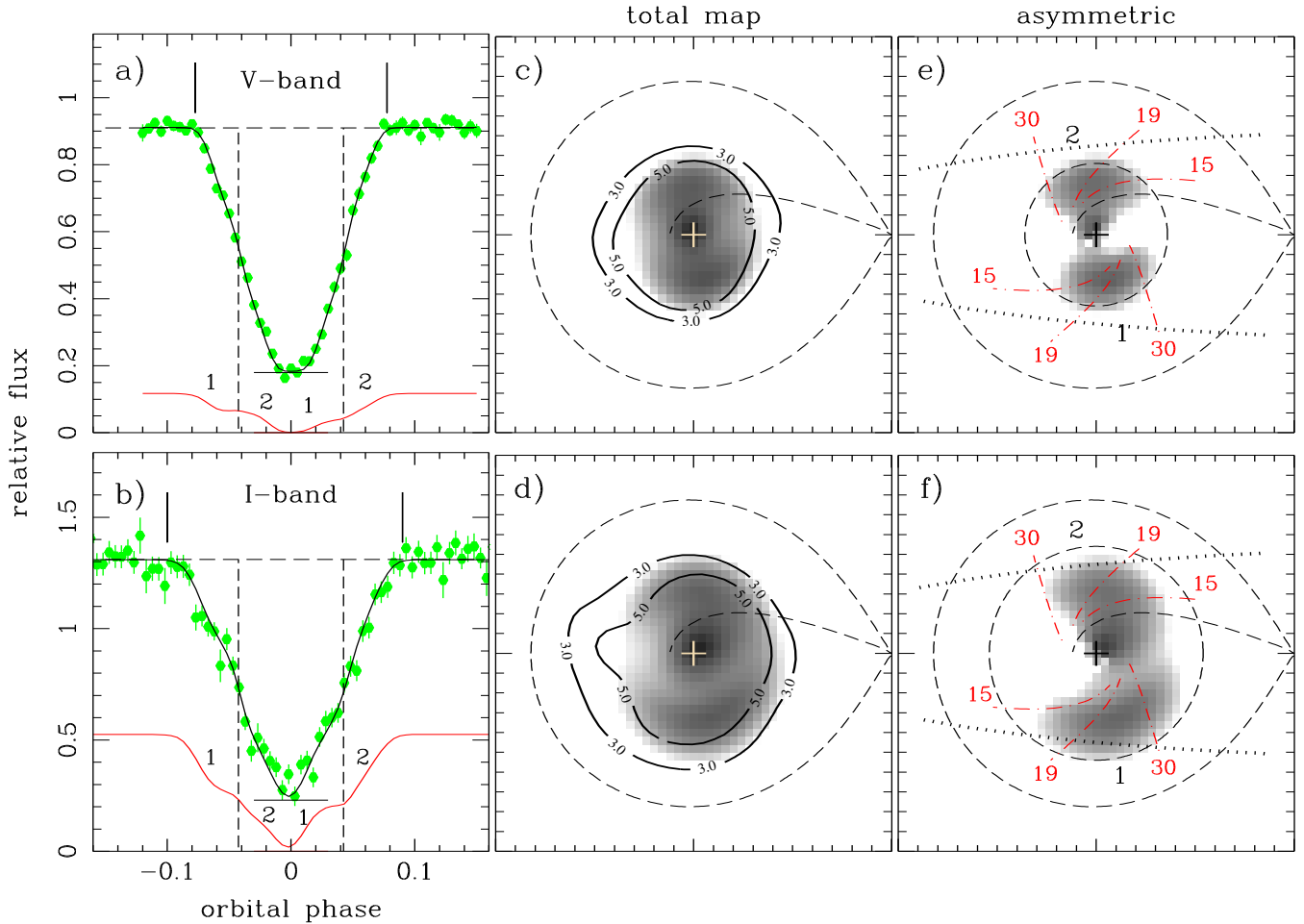


Figure 3. Left-hand panels: average data (green points with error bars) and best-fit eclipse mapping model (solid line) for the V-band (a) and I-band (b) light curves. Horizontal bars at mid-eclipse show the unclipped flux **in each case**. Vertical dashed lines mark the best-fit $\Delta\phi$ value (indicating the WD ingress/egress phases), and vertical ticks mark the total width of the eclipse, $\Delta\phi_E$. The lower red curve illustrates the eclipse light curve of the asymmetric arcs 1 and 2 (see text). Middle panels: V-band (c) and I-band (d) eclipse maps in a logarithmic grayscale; darker regions are brighter. Regions inside the two solid contour lines are above the 3σ and 5σ confidence levels, respectively. A cross marks the position of the disk center; dashed lines depict the primary Roche lobe and the gas stream trajectory. Right-hand panels: The asymmetric component of the V-band (e) and I-band (f) eclipse maps in a logarithmic grayscale. Dashed circles mark the estimated disk radii; dotted lines show the edge of the projected shadow of the secondary star at phase zero, while dot-dashed red lines illustrate the expected orientation of tidally-induced spiral arms for constant opening angles of $\theta_s = 15^\circ$, 19° , and 30° . The location of asymmetric arcs 1 and 2 is indicated.

The uncertainties in the eclipse map were derived from Monte Carlo simulations with the average eclipse light curve, generating a set of 20 randomized eclipse maps (see Rutten et al. 1992). These are combined to produce a map of the standard deviations with respect to the true map. A map of the statistical significance (or the inverse of the relative error) is obtained by dividing the true eclipse map by the map of the standard deviations (Baptista et al. 2005). The uncertainties obtained with this procedure are used to plot the confidence level contours of the eclipse maps in the middle panels of Fig. 3

and to estimate the uncertainties of the azimuthal distributions of Fig. 4.

The solid lines in the left-hand panels of Fig. 3 are the eclipse light curves resulting from the best fit eclipse maps depicted on a logarithmic grayscale in the middle panels of Fig. 3. The orientation of the eclipse map is such that the secondary star rotates counter-clockwise around the WD at the center of the map (in the observer's reference frame), while the observer rotates clockwise (in the binary reference frame). At phase zero, the secondary and the observer are on the right side

of the map (with the projected shadow of the secondary star completely covering the disk). At phase +0.25 the observer is at the bottom (in the binary frame) while the secondary star is at the top of the eclipse map (in the observer’s frame).

The eclipse maps in the middle panels of Fig. 3 show no evidence of a bright spot at the disk rim, and no enhanced emission along the gas stream trajectory. The statistical significance of the surface brightness distributions is above the 5σ confidence level. In the V-band, the accretion disk is small and fills less than half of the primary Roche lobe. From the measured total eclipse duration of $\Delta\phi_E = 0.156 \pm 0.001$ in phase, its radius is estimated to be $R_d/R_{L1} = 0.36$. The I-band eclipse is wider, with $\Delta\phi_E = 0.200 \pm 0.005$, which leads to a larger estimated radius of $R_d/R_{L1} = 0.54$, 50 per cent larger than in the V-band. This is in line with the expected behavior of an opaque steady-state disk, in which the temperature drops with distance from disk center as $T(R) \propto R^{-3/4}$.

The right-hand panels of Fig. 3 show the asymmetric component of the eclipse maps, obtained by slicing the disk in a set of radial bins and by fitting a smooth spline function to the median of the lower half of the intensities in each bin. Then the spline-fitted intensity in each bin is subtracted from the total intensity. This procedure essentially separates the baseline of the radial profile from the azimuthal structures into symmetric and asymmetric maps, respectively. A dashed circle shows the inferred disk radius in each case. Dotted lines depict the shadow of the secondary star at phase zero, indicating that in the V-band the disk is fully eclipsed at this phase. Given that all V-band light from the accretion disk is occulted at phase zero, the remaining flux at that phase cannot be accommodated in the eclipse map and is dumped into the uneclipsed flux component. We find a significant uneclipsed component of 20 per cent of the total out-of-eclipse V-band flux (indicated by the horizontal bar at mid-eclipse in Fig. 3a).

4.2. *Spiral structures*

Apart from the central brightness enhancement, both in the V-band and in the I-band the accretion disk is elongated in the direction perpendicular to the line joining both stars and displays two asymmetric, arc-shaped sources of comparable brightness, located in the lower right (arm 1) and upper left (arm 2) quadrants of the eclipse maps in Fig. 3. The arcs show an azimuthal extent of $\sim 90^\circ$, extend from intermediate ($R \simeq 0.2 R_{L1}$) to outer disk regions, and represent a significant fraction of the emitted light. They account for 33 per cent of the total out-of-eclipse flux (or 40 per cent of the disk flux)

in the V-band and for 40 per cent of the total out-of-eclipse flux (or 48 per cent of the disk flux) in the I-band. These features resemble the asymmetric structures observed in the eclipse maps of IP Peg (Baptista et al. 2000, 2002, 2005), V348 Pup (Saito & Baptista 2016) and V2051 Oph (Baptista & Wojcikiewicz 2020), which have been interpreted as spiral shocks in the outer disk regions, induced by tidal forces from the secondary star (Sawada et al. 1986a; Boffin 2001; Steeghs 2001). For more details, see Sect. 5.2.

To investigate the properties of the asymmetric arcs, we followed the method of Baptista et al. (2000). We divided the eclipse map into azimuthal slices (i.e., “pizza slices”) and computed the radius at which the intensity reaches a maximum for each azimuth. A corresponding Keplerian velocity is computed for the radius of maximum intensity, assuming $M_1 = 0.66 M_\odot$ and $R_{L1} = 0.72 R_\odot$ (see Sect. 5). This exercise allows us to recover the location of the spiral structures both in radius and in azimuth (e.g., Baptista et al. 2000, 2005). The results are shown in Fig. 4 as a function of binary phase. The distribution of the maximum intensity $I_{\max}(\phi)$ from the azimuthal slices and the corresponding radius $R(I_{\max})$, are shown in the upper and lower panels, respectively. The uncertainties in these two quantities are obtained from the Monte Carlo simulations described in Sect. 4.1. Orbital phases are measured from the line connecting the two stars and increase in the clockwise direction (Fig. 3). The two-armed asymmetric structures lead to a double-humped shape in the intensity distribution, with the maxima indicating the azimuthal positions of arms 1 and 2. In the V-band, arms 1 and 2 lay at a comparable distance of $R \simeq 0.26 R_{L1}$ from the disk center (expected Keplerian velocities of about 800 – 840 km/s); in the I-band, Arm 1 is farther away, at $R \simeq 0.35 R_{L1}$ (corresponding to Keplerian velocities of $\simeq 690 - 720$ km/s). These velocities, corresponding to a location not far from the outer disk edge, should be lower than the velocity determined from the integrated disk light. They are thus compatible with FWHM of 1130 km/s (1260 km/s) of the $H\alpha$ ($H\beta$) emission lines reported by Oliveira et al. (2020). Dashed lines in the lower panel of Fig. 4 depict the circularization radius for $q = 0.45$ ($R_{\text{circ}} = 0.208 R_{L1}$) and the estimated outer disk radius in each band. The two-armed structures are within these two limits. Spiral shocks are expected to exhibit sub-Keplerian velocities, with a velocity reduction that can be as large as 30 per cent (e.g., Baptista et al. 2000). If this is the case, the hot, post-shock, line emitting gas is expected to appear as arc-shaped structures at velocities of $\simeq 550$ km/s in Doppler tomograms.

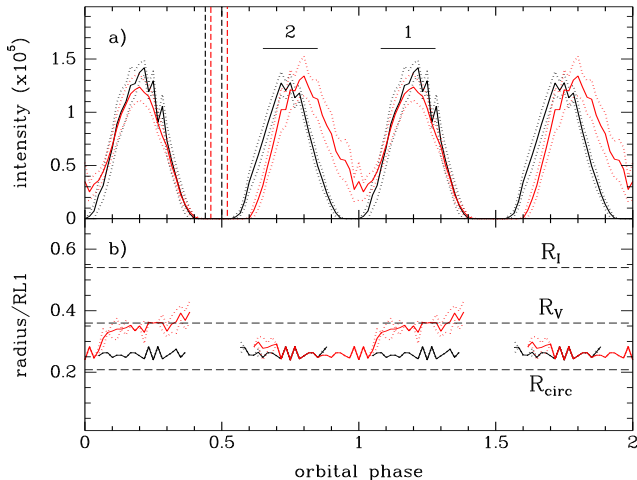


Figure 4. *a)* Dependency on orbital phase of the maximum intensity derived from the asymmetric component of the V-band (black) and I-band (red) eclipse maps. Intensities are plotted on an arbitrary scale; arms 1 and 2 are labeled and horizontal tick marks indicate the phases of maxima of the double-wave orbital modulation. Dotted lines show the uncertainties at the 1σ limit. Vertical dashed lines mark the $1\text{-}\sigma$ range of values for the phase of lowest intensity, $\phi_1(I_{\min})$ (see text). *b)* Corresponding radius of maximum intensity in units of R_{L1} . Horizontal dashed lines mark the circularization radius ($R_{\text{circ}} = 0.208 R_{L1}$) and the outer disk radius ($R_V = 0.36 R_{L1}$ in the V-band and $R_I = 0.54 R_{L1}$ in the I-band).

5. DISCUSSION

5.1. Basic system parameters

We have detected eclipses in the nova-like CV CRTS J0934 through phase-resolved ground and space-based optical observations spanning more than six years. These eclipses permit a high-precision measurement of the system’s orbital period. At about 3.92 h, it falls within the typical range for nova-like variables.

A detailed analysis of the average eclipse profile using eclipse mapping techniques reveals further details of the structure of CRTS J0934. It turns out that the V-band accretion disk radius of $R_V/R_{L1} = 0.36$ is relatively small compared to that of other nova-like CVs. The approximations of Plavec & Kratochvil (1964) and Eggleton (1983) together with the mass ratio of 0.45 yield a volume equivalent radius of the WD Roche lobe of $R_{1,\text{eq}} = 0.78 R_{L1}$. The CRTS J0934 disk radius is then $0.46 R_{1,\text{eq}}$. Harrop-Allin & Warner (1996) determined the disk radii in 25 nova-like variables and old novae, finding values ranging between $0.46 \leq R_d/R_{1,\text{eq}} \leq 0.95$. Thus, the V-band radius of the CRTS J0934 disk lies at the lower edge of the disk radii range measured by Harrop-Allin & Warner (1996).

The small V-band disk radius, combined with the high orbital inclination of 81.5° , accounts for the faint optical absolute magnitude of $M_g = 7.44 \pm 0.57$ derived for the system. This value was obtained from the average apparent magnitude of $g = 18.69 \pm 0.28$, assuming a distance of 1646^{+457}_{-301} pc (Bailer-Jones et al. 2021) and an interstellar extinction of $A_V = 0.159$, using the 3D extinction maps of Doroshenko (2024) together with a ratio $A_V/A_g = 0.94$ (Schlafly & Finkbeiner 2011). Applying the correction suggested by Paczyński & Schwarzenberg-Czerny (1980) to adjust the disk magnitude to the average inclination (while neglecting any contribution from the secondary star to the total light) yields an absolute magnitude of $M_{g,\text{corr}} = 5.72 \pm 0.57$. Reflecting the effect of the small V-band disk radius, this value lies at the faint end of the absolute magnitude distribution of novalike variables above the CV period gap (Bruch 2024b).

Some important system parameters have already been derived in the preceding sections. Others can be inferred based on reasonable assumptions. They are listed in Table 4. The fundamental assumption concerns the mass of the secondary star, which is taken to be $M_2 = 0.297 M_\odot$, according to the empirical relation between orbital period and M_2 of Knigge et al. (2011). We adopted a conservative uncertainty of 20 per cent to the M_2 estimate. Together with the adopted mass ratio, this yields a WD mass of $M_1 = 0.66 M_\odot$. The component separation a follows from Kepler’s third law. The approximation of Plavec & Kratochvil (1964) for R_{L1}/a then yields the distance between the WD and the L1 point. The mass-radius relation for WDs of Nauenberg (1972) provides the radius of the primary star, while R_2 is taken as the volume equivalent Roche lobe radius of the secondary star, following Eggleton (1983). The outer disk radius is estimated from the measured total eclipse duration (Sect. 4.1). Standard error propagation and Monte Carlo simulations with 10^5 trials on the input parameters q , M_2 and $\Delta\phi_E$ is used to estimate the uncertainties of the remaining binary parameters.

Our eclipse mapping revealed that about 20 per cent of the total V-band out-of-eclipse flux remains uneclipsed. The source of this extra light cannot be in the orbital plane. For a secondary star mass of $0.297 M_\odot$, Knigge et al. (2011) list an absolute magnitude of $M_V = 10.93$. Comparing this to the absolute magnitude of the entire system of $M_g = 5.72$, it is obvious that the secondary star can account for only a small fraction of the uneclipsed light. This could be different if the secondary were evolved. To fit in the Roche-lobe of a ~ 4 h binary, it then must have been stripped of its outer layers, exposing its hotter interior. Depending on the degree of

Table 4. System parameters for CRTS J0934

orbital period	P_{orb}	$0.16329188 \pm 0.00000008$ d
apparent magnitude ^a	m_g	18.69 ± 0.28
absolute magnitude ^a	M_g	7.44 ± 0.57
distance ^b	d	1645 ± 379 pc
orbital inclination	i	$81.5^\circ \pm 1.0^\circ$
component separation	a	$1.238 \pm 0.088 R_\odot$
distance WD – L1	R_{L1}	$0.716 \pm 0.059 R_\odot$
accretion disk radius	R_V	$0.36 \pm 0.01 R_{L1}$
	R_I	$0.54 \pm 0.05 R_{L1}$
mass ratio	q	0.45 ± 0.05
primary star mass	M_1	$0.66 \pm 0.15 M_\odot$
primary star radius	R_1	$0.012 \pm 0.002 R_\odot$
secondary star mass	M_2	$0.297 \pm 0.059 M_\odot$
secondary star radius	R_2	$0.386 \pm 0.027 R_\odot$
rad. vel. amplitude	K_1	118 ± 10 km/s
	K_2	262 ± 24 km/s

^a: average out-of-eclipse magnitude in high state

^b: Bailer-Jones et al. (2021)

stripping, nuclear processed matter may then be transferred to the primary component. A detailed spectroscopic analysis may confirm or discard this hypothesis. Alternatively, most of the uneclipsed light may have a different origin, such as, for instance, a vertically extended disk wind.

5.2. *Spiral shocks*

Another noteworthy feature is the presence of two asymmetric arcs in the accretion disk. Numerical simulations by Meglicki et al. (1993) reveals that stream-disk interaction may lead to thickenings of the disk rim at the orbital phases $\phi \sim 0.2, 0.5$ and 0.8 , which could appear in eclipse maps as arcs of enhanced emission due to the reprocessing of radiation from the inner disk. However, this is not a plausible explanation for the observed asymmetric arcs because (i) there is no conspicuous bright spot at the disk rim and no enhanced emission along the gas stream trajectory to signal any relevant stream-disk interaction, (ii) there is no asymmetric structure at phase 0.5 and (iii) the asymmetric arcs are well within the disk (at $R \simeq 0.75 R_d$) and not at its rim.

Alternatively, Smak (2001) and Ogilvie (2002) proposed that these asymmetric arcs are caused by irradiation of tidally thickened sectors of the outer disk by the hot, inner disk regions. However, eclipse mapping results offer no support for these explanations (Baptista et al. 2005). First, the eclipse mapping procedure projects any emission produced at height z above the disk back along the inclined line of sight to the

point where it pierces the disk plane, at a distance $z \tan i$ away from the secondary star with respect to its true position (Baptista et al. 1995). For a high inclination system such as CRTS J0934, even a small vertical height $z \simeq 0.03 R_{L1} = 1.5 \times 10^9$ cm would be enough to shift both arms by $\Delta x \simeq 0.2 R_{L1}$ towards the secondary star with respect to their positions in the eclipse maps. The resulting highly asymmetric geometrical configuration would be inconsistent with the framework of tides induced by the secondary star, which are point-symmetric with respect to the WD both for the shocks (Steehgs & Stehle 1999; Makita et al. 2000) and the irradiation (Smak 2001; Ogilvie 2002) interpretations. Second, the irradiation model predicts that irradiation affects mainly the side of the thickened disk facing the hot inner regions. When the thickened disk structure is viewed from a highly inclined line of sight towards the secondary star (i.e., around eclipse) the irradiated arm 2 would be seen mostly face-on, but arm 1 would suffer self-occultation (or would be seen at a much lower effective area). Thus, in the irradiation model one expects that arm 2 appears systematically (and possibly significantly) brighter than arm 1 around eclipse (and this brightness difference would be transported to any eclipse map) – which is not supported by eclipse mapping results (Baptista et al. 2005).

The remaining explanation is that the asymmetric arcs are tidally-induced spiral shocks in the accretion disk. Numerical calculations by Sawada et al. (1986a,b) predicted that the tidal action of the secondary star leads to accretion disks elongated in the direction perpendicular to the line joining both stars, with the appearance of a two-armed spiral shock wave in its outer regions which propagates to small radii roughly at the local sound speed, c_s (e.g., Boffin 2001). In an inviscid disk, the opening angle of the spiral arms (i.e., the angle between the shock surface and the direction of the orbital motion) is of the order of $\tan \theta_s = c_s/v_\phi$ where v_ϕ is the local Keplerian velocity (e.g., Różyczka & Spruit 1989). Observational evidence of such spiral arms were found in the accretion disk of the dwarf nova IP Peg during outbursts (Steehgs et al. 1997; Harlaftis et al. 1999; Baptista et al. 2000, 2002). The comparison between the velocities (Doppler tomography) and locations (eclipse mapping) reveal that the spiral pattern extends significantly inwards of the accretion disk (down to $\simeq 0.2 R_{L1}$) and that the observed (Doppler) velocities are up to 30 per cent lower than the corresponding Keplerian velocities, underscoring the shock nature of these structures. At the time of the above mentioned studies, the lack of clear evidence of spiral structures in the accretion disks of nova-likes and quiescent dwarf novae

fostered the idea that, in order to excite the tidally-induced spiral pattern, the accretion disk needs to be exceedingly large such as during dwarf nova outbursts.

Subsequent numerical simulations and observations led to a different picture. Armitage & Murray (1998) attempted to reproduce the spiral arms in the accretion disk of IP Peg. The tidally-induced spiral pattern appears in both the quiescent and outburst cases. The opening angle of the spirals increases when the disk viscosity parameter α^6 is increased by a factor of 4, from $\alpha = 0.15$ in quiescence to $\alpha = 0.6$ in outburst, and matches those observed in IP Peg. Stehle (1999) consistently found tidally-induced spiral structures in accretion disk simulations for both the assumed “quiescence” (low $\alpha = 0.01$) and “outburst” (high $\alpha = 0.3$) cases. Low viscosity leads to tightly wound spiral arms, while high viscosity results in wide open spiral arms such as those observed. As a consequence of the increased viscosity, his “outburst” disk becomes ~ 10 per cent larger than in “quiescence”. Makita et al. (2000) and Sato et al. (2003) investigated tidally-induced spiral structures from “cool” ($\gamma = 1.01$) to “hot” ($\gamma = 5/3$) accretion disks. Spiral patterns are present in all cases, regardless of outer disk radius. Smaller γ values (lower temperatures) resulted in a more tightly wound spiral pattern, and the spiral shock waves only disappeared when the tidal force from the secondary star was artificially cut off. Wide open spirals such as those observed are obtained when radiative cooling is taken into account. The summary of the numerical simulations is that tidally-induced spiral pattern is always present in an accretion disk; its opening angle is large in hot and/or high-viscosity disks (leading to wide open spiral arms easier to detect observationally) and small in cool and/or low-viscosity disks (leading to tightly wound spirals which become indistinguishable from the underlying accretion disk; e.g., Steeghs & Stehle 1999). Observational support for this picture comes from the results of Baptista et al. (2005), who found that the opening angle of the spiral arms in IP Peg progressively decreases while its accretion disk cools during outburst decline. The further discovery of spiral arms in the accretion disks of the quiescent dwarf nova V2051 Oph (Rutkowski et al. 2016; Baptista & Wojcikiewicz 2020) and of the nova-like systems V347 Pup (Thoroughgood et al. 2005), V348 Pup (Saito & Baptista 2016) and EC21178 (Khangale et al. 2020; Ruiz-Carmona et al. 2020) allows a crucial test of

the idea that an exceedingly large disk is required in order to excite the spiral pattern.

For eclipsing systems, the width of the eclipse $\Delta\phi_E$ can be used to estimate the disk radius (e.g., Baptista & Wojcikiewicz 2020) and to compare it with the tidal truncation radius R_T (Paczynski 1977),

$$\frac{R_T}{R_{L1}} = \frac{0.6}{(1+q)} \frac{a}{R_{L1}}, \quad (2)$$

where $R_{L1}/a = 0.5 - 0.227 \log q$ (Plavec & Kratochvil 1964). For V347 Pup ($q = 0.83 \pm 0.05$, $\Delta\phi_E = 0.110 \pm 0.005$, Thoroughgood et al. 2005) we find $R_d/R_T = 0.86$, for V348 Pup ($0.31 \leq q \leq 0.6$, $\Delta\phi_E = 0.087 \pm 0.002$, Saito & Baptista 2016) we obtain $R_d/R_T \simeq 0.7$, and for EC21178 ($q = 0.48 \pm 0.06$, $\Delta\phi_E = 0.092 \pm 0.003$, Khangale et al. 2020) we find $R_d/R_T \simeq 0.7$ as well. CRTS J0934 fits nicely into this group, with an estimated $R_I/R_T = 0.75$. Furthermore, the quiescent dwarf nova V2051 Oph ($q = 0.19 \pm 0.03$, $\Delta\phi_E = 0.082 \pm 0.003$, Baptista & Wojcikiewicz 2020) provides an extreme case with $R_d/R_T = 0.56$. The results show that these accretion disks are not particularly large and do not extend up to the region of strong gravitational perturbation from the secondary star, indicating that disk size is not a determining factor for the presence of spiral arms.

While it is not possible to estimate the opening angle of the spirals directly from the eclipse map⁷, their orientation (i.e., binary phase ϕ_s) and azimuthal extent $\Delta\phi_s$ are well recovered. There is a clear correlation between θ_s and $(\phi_s, \Delta\phi_s)$: wide open spirals with large opening angles are mapped as arcs of small azimuthal extent at an orientation roughly perpendicular to the line joining both stars; ϕ_s and $\Delta\phi_s$ both increase as θ_s decreases and the spirals wind up. This correlation led Baptista et al. (2005) to devise an indirect way to estimate θ_s from the orientation of the valleys in the azimuthal intensity distribution, which rotate clockwise as the opening angle decreases. They found that the orbital phase of lowest intensity (the valley) in the azimuthal intensity distribution correlates to the opening angle of the spirals through the expression,

$$\theta_s(\text{degrees}) = \frac{23.25}{\phi_1(I_{\min})} - 29.6, \quad (3)$$

⁶ Here we adopt the notation of Shakura & Sunyaev (1973) and write the disk viscosity as $\nu = \alpha c_s H$, where H is the disk vertical scaleheight.

⁷ As a consequence of the intrinsic azimuthal smearing effect of the eclipse mapping method, spiral arms are smeared in the azimuthal direction; their trace in the azimuthal intensity distribution tends to be at a constant average radius, which cannot be used to estimate the opening angle θ_s of the spirals (Harlaftis et al. 2004).

where $\phi_1(I_{\min})$ corresponds to the first of the two orbital phases of intensity valleys in the azimuthal intensity distribution. We fitted a parabola to the intensities around the first valley of the azimuthal intensity distributions of Fig. 4a to find an average value of $\phi_1(I_{\min}) = 0.47 \pm 0.04$. This leads to an average opening angle of $\theta_s = 19^\circ \pm 4^\circ$. This estimate can be visually checked against the expected trace of tidally-induced spiral arms for opening angles of $\theta_s = 15^\circ, 19^\circ$ and 30° (shown as dot-dashed red lines) in the right-hand panels of Fig. 3. Spiral arms with $\theta_s = 30^\circ$ ($\theta = 15^\circ$) underestimate (overestimate) the orientation and azimuthal extent of the observed asymmetric structures, while that with $\theta_s = 19^\circ$ provides a reasonably good match to the binary phases and azimuthal extent of the observed asymmetric structures. The θ_s value obtained for CRTS J0934 is comparable to that inferred for the spirals in the quiescent accretion disk of V2051 Oph ($\theta_s = 21^\circ \pm 3^\circ$, Baptista & Wojcikiewicz 2020) and 5-6 d after of the onset of the outburst in IP Peg ($\theta_s = 25^\circ \pm 3^\circ$, Baptista et al. 2005).

The detection of wide open spiral density waves in the nova-like CRTS J0934 suggests that its accretion disk has a high mass accretion rate (and, therefore, high temperatures) and/or a high viscosity. Both characteristics are typical of novalike systems close to the upper side of the CV period gap.

6. SUMMARY

Using long-term photometric observations combined with time-resolved light curves of the variable star CRTS SSS100505 J093416-174421, we provide the first detailed characterization of this system. We identify it as an eclipsing nova-like cataclysmic variable of the VY Scl subtype with an orbital period of 0.16329188 d (3.919005 h). Tomography of the eclipse profile shows us that the accretion disk is completely eclipsed. Residual emission at mid-eclipse may be due to matter above or below the orbital plane, with only a small contribution from a main sequence secondary star. We find best fit values of $81.5^\circ \pm 1.0^\circ$ for the orbital inclination and a mass ratio of $q = 0.45 \pm 0.05$. This, together with reasonable assumptions, allowed us to estimate further system parameters. Even being total, the eclipses are rather brief. This is due to an accretion disk that is smaller than observed in other nova-like variables. Its outer radius is only 21 per cent of the component separation or 36 per cent of the distance between the WD and the L1 point when observed in the V-band. However, seen in the near infrared, it increases to 0.54 of the WD-L1 distance. The small V-band disk combined with the

high inclination explains the faint absolute magnitude of $M_g = 7.44$ which is close to the faint end of the absolute magnitude distribution for nova-like CVs. The eclipse tomography also reveals the presence of two asymmetrical structures in the disk that can be interpreted as tidally-induced spiral arms.

ACKNOWLEDGEMENTS

This paper is largely based on observations carried out at the Observatório do Pico dos Dias (OPD), operated by the Laboratório Nacional de Astrofísica (LA/MCTI, Brazil, under OPD observing program 2021A-P-04 (PI: A. Bruch). Supportive observations from TESS, CRTS, and ZTF were also used. Data from the TESS space mission were downloaded from the MAST data archive at the Space Telescope Science Institute (STScI). Funding for the mission is provided by the NASA Explorer Program. STScI is operated by the Association of Universities for Research in Astronomy, Inc., under NASA contract NAS 5-26555. CRTS is supported by the US NSF under grants AST-0909182 and CNS-0540369. The work at Caltech was supported in part by the NASA Fermi grant 08-FERMI08-0025, and by the Ajax Foundation. The CSS survey is funded by the National Aeronautics and Space Administration under grant no. NNG05GF22G issued through the Science Mission Directorate Near-Earth Objects Observations Programme. ZTF observations are carried out with the Samuel Oschin 48-inch and the 60-inch Telescope at the Palomar Observatory as part of the Zwicky Transient Facility project. ZTF is supported by the National Science Foundation under Grants No. AST-1440341 and AST-2034437, and a collaboration including Caltech, IPAC, the Weizmann Institute for Science, the Oskar Klein Center at Stockholm University, the University of Maryland, the University of Washington, Deutsches Elektronen-Synchrotron and Humboldt University, Los Alamos National Laboratories, the TANGO Consortium of Taiwan, the University of Wisconsin at Milwaukee, Trinity College Dublin, Lawrence Berkeley National Laboratories, Lawrence Liverpool National Laboratories, and IN2P3, France. Operations are conducted by COO, IPAC, and UW. R.L.O. was partially supported by CNPq (PQ-315632/2023-2 and 445047/2024-0) and FAPESP (2025/01204-6). C.V.R. thanks the support from the Brazilian Space Agency (PO 20VB.0009) and CNPq (305991/2024-8). A.S.O. acknowledges the support from FAPESP (2017/20309-7). I.J.L. thanks FAPESP (grant #2024/14358-9 and #2024/03736-2).

REFERENCES

- Armitage, P.J. & Murray, J.R. 1998, *MNRAS*, 297, L81
- Bailer-Jones, C.A.L., Rybizki, J., Fouesneau, M., Demleitner, M., & Andrae, R. 2021, *AJ*, 161, 147
- Bailey, J. 1979, *MNRAS*, 187, 645
- Baptista, R. 2001, in: H.M.J. Boffin, C. Steeghs, & J. Cypers, eds., *Lecture Notes in Physics*, Vol. 573, *Astrotomography, Indirect Imaging Methods in Observational Astronomy*, Springer Verlag, Berlin, p. 307
- Baptista, R. 2016, *Astronomy at High Angular Resolution, Astrophysics and Space Science Library*, Vol. 439 Springer International Publishing, Switzerland, p. 155
- Baptista, R., Horne, K., Hilditch, R., Mason, K. O., & Drew, J. E., 1995, *ApJ*, 448, 395
- Baptista, R., Borges, B.W., & Oliveira, A.S. 2016, *MNRAS*, 463, 3799
- Baptista, R., Harlaftis, E.T., & Steeghs, D. 2000, *MNRAS*, 314, 727
- Baptista, R., Haswell, C.A., & Thomas, G. 2002, *MNRAS*, 334, 198
- Baptista, R., Morales-Rueda, L., Harlaftis, E.T., Marsh, T.R., & Steeghs, D. 2005, *A&A*, 444, 201
- Baptista, R., & Wojcikiewicz, E. 2020, *MNRAS*, 492, 115
- Bellm, R.C., Kulkarni, S.R., Graham, M.J., et al. 2019, *PASP*, 131, 995, 018002
- Boffin, H.M.J. 2001, in: H.M.J. Boffin, C. Steeghs, & J. Cypers, eds., *Lecture Notes in Physics*, Vol. 573, *Astrotomography, Indirect Imaging Methods in Observational Astronomy*, Springer Verlag, Berlin, p. 69
- Briggs, G.P., Ferrario, L., Tout, C.H., & Wickramasinghe, D.T. 2018, *MNRAS*, 481, 3604
- Bruch A., 2018, *New Astr.*, 58, 53
- Bruch, A. 2021, *MNRAS*, 503, 953
- Bruch, A. 2024a, *ApJS*, 273, 6
- Bruch, A. 2024b, *ApJ*, 977, 153
- Doroshenko, V. 2024, *arXiv*, 240303127
- Drake, A.J., Djorgovski, S.G., Mahabal, A., et al. 2009, *ApJ*, 696, 870
- Duffy, C., Wu, K., Ramsay, G., et al. 2024, *MNRAS*, 535, 3035
- Eastman, J., Siverd, R., & Gaudi B.S. 2010, *PASP*, 122, 935
- Eggleton, P.P. 1983, *Apj*, 268, 368
- Harlaftis, E.T., Steeghs, D., Horne, K., Martin, E., & Magazzu, A., 1999, *MNRAS*, 306, 348
- Harlaftis, E., Baptista, R., Morales-Rueda, L., Marsh, T.R. & Steeghs, D. 2004, *A&A*, 417, 1063
- Harrop-Allin, M.K., & Warner, B. 1996, *MNRAS*, 279, 219
- Horne, K. 1985, *MNRAS*, 213, 129
- Khangale, Z. N., Woudt, P. A., & Potter, S. B. et al., 2020, *MNRAS*, 495, 637
- Knigge, C., Baraffe, I., & Patterson, J. 2011, *ApJS*, 194, 28
- Kochanek, C.S., Shappee, B.J., Stanek, K.Z., et al. 2017, *PASP*, 129, 104502
- Leach, R., Hessman, F.V., King, A.R., Stehle, R., & Mattei, J. 1999, *MNRAS*, 305, 225
- Makita, M., Miyawaki, K., & Matsuda, T. 2000, *MNRAS*, 316, 906
- Marsh, T. 2001, in: H.M.J. Boffin, C. Steeghs, & J. Cypers, eds., *Lecture Notes in Physics*, Vol. 573, *Astrotomography, Indirect Imaging Methods in Observational Astronomy*, Springer Verlag, Berlin, p. 1
- Masci, F.H., Laher, R.R., Rusholme, B., et al. 2019, *PASP*, 131, 018003
- Matsuda, T., Makita, M., & Fujiwara, H. 2000, *Ap&SS*, 274, 259
- Meglicki, Z., Wickramasinghe, D. T., Bicknell, G. V., 1993, *MNRAS*, 264, 691
- Nauenberg, M. 1972, *ApJ*, 175, 417
- Ogilvie, G.I., 2002, *MNRAS*, 330, 937
- Oliveira, A.S, Rodrigues, C.V., Martins, M., et al. 2020, *AJ*, 159, 114
- Paczysński, B., 1977, *ApJ*, 216, 822
- Paczysński, B., & Schwarzenberg-Czerny, A. 1980, *AcA*, 20, 127
- Plavec, M., & Kratochvil, P. 1964, *Bull. Astr. Czech.*, 15, 165
- Ricker, G.R., Winn, J.N., Vanderspek, R., et al. 2014, *J. Astr. Tel. Instr. & Systems*, 1, 014003
- Robinson, E.L. 1976, *ARAA*, 14, 119
- Różyczka, M., & Spruit, H.C., 1989, in *Theory of Accretion Disks*, ed. F. Meyer et al. (Dordrecht, Kluwer), 351
- Ruiz-Carmona, R., Khangale, Z. N., Woudt, P. A., & Groot, P. J., 2020, *MNRAS*, 491, 344
- Rutkowski, A., Waniak, W., Preston, G., & Pych, W., 2016, *MNRAS*, 463, 3290
- Rutten, R.G.M., van Paradijs, J. & Tinbergen, J. 1992, *A&A*, 260, 213
- Saito, R. K., & Baptista, R., 2016, *MNRAS*, 457, 198
- Sato, J., Sawada, K., & Ohnishi, N. 2003, *MNRAS*, 342, 593
- Savitzky, A., & Golay, M.J.E. 1964, *Analytical Chemistry*, 36, 1627
- Sawada, K., Matsuda, I., & Hachisu, I. 1986a, *MNRAS*, 219, 75
- Sawada, K., Matsuda, I., & Hachisu, I. 1986b, *MNRAS*, 221, 679 75
- Schaefer, B.E. 2024, *ApJ*, 966, 155
- Schlafly E.F., & Finkbeiner, D.P. 2011, *ApJ*, 737, 103
- Schreiber, M.T., Belloni, D., Gänsicke, B.T., Parsons, S.G., & Zorotovic, M. 2021, *NatAs*, 5, 648

- Silber, A.D. 1992, Studies of an X-ray Selected Sample of Cataclysmic Variable, PhD thesis, Massachusetts Institute of Technology
- Shakura, N.I., & Sunyaev, R. 1973, *A&A*, 24, 337
- Smak, J.I., 2001, *Acta Astron.*, 51, 295
- Spruit, H.C. 1994, *A&A*, 289, 441
- Steeghs, D. 2001, in: H.M.J. Boffin, C. Steeghs, & J. Cypers, eds., *Lecture Notes in Physics*, Vol. 573, *Astrotomography, Indirect Imaging Methods in Observational Astronomy*, Springer Verlag, Berlin, p. 45
- Steeghs, D., Harlaftis, E.T., & Horne, K. 1997, *MNRAS*, 290, L28
- Steeghs, D., & Stehle, R., 1999, *MNRAS*, 307, 99
- Stehle, R. 1999, *MNRAS*, 304, 687
- Thoroughgood, T. D., Dhillon, V. S., Steeghs, D. et al., 2005, *MNRAS*, 357, 881
- Warner, B. 1976, *IAU Symp. 73, Structure and Evolution of Close Binary Systems*, ed. P. Eggleton, S. Mitton, & J. Whelan (Dordrecht, D. Reidel Publishing Company), 85
- Warner, B., 1995, *Cataclysmic Variable Stars*, Cambridge University Press, Cambridge
- York, D.G., Adelman, J., Anderson, J.E., et al. 2000, *AJ*, 120, 1579
- Zacharias, N., Finch, C.T., Girard, T.M., et al. 2013, *AJ*, 145, 44
- Zorotovic, M., & Schreiber, M.R. 2020, *AdSpR*, 66, 108
- Zorotovic, M., Schreiber, M.R., & Gänsicke, B.T. 2011, *A&A*, 536, A42